ISSN No:-2456-2165

Designing a Special Nozzle for Cold Spray Additive Manufacturing of Ti6Al4V using Numerical Simulation and Experimental Validation

Er. Aashutosh Singh[1] , Er. Snil Prabhakar[2], Er. Shweta Mishra[3]
[1]Student, [2,3]Assistant Professor
Department of Mechanical Engineering, Institute of Engineering & Technology,
Dr. Rammanohar Lohia Avadh University, Ayodhya – 224001

Abstract:- Cold splash added substance fabricating shows extraordinary potential of titanium-composite creation as. It's a strong state of process. Nonetheless, information distributed so far has exhibited the trouble of creating thick and high-strength Ti combination parts. Our past examinations have shown that spout configuration along with significant expense helium propulsive gas assumes a urgent part in molecule speed increase. In this work, unique spouts for Ti composite were planned and approved tentatively with economically accessible Ti6Al4V powder. Reenactment results show that molecule influence temperature increments surprisingly for a long merged length, while molecule motor energy somewhat expands, which is approved by tests. The connection between the molecule influence temperature and practice width shows the main increment and afterward decline. The trial results show that as the spout concurrent area turns out to be longer, the edges of the single-pass stores become smoother, and the width, thickness, statement effectiveness, and microhardness of the single-pass stores increment.

Keywords:- *Cold shower; Ti6Al4V compound; added substance fabricating; Laval spout; affidavit proficiency.*

I. INTRODUCTION

Cold splash added substance producing (CSAM), which has created from the virus shower (CS) covering process, is another individual from the added substance fabricating advances. It depends on the strong state testimony of seriously twisted powder particles that influence a substrate at high rates to frame a store. It contrasts from customary warm splashing, as it is accomplished at much lower temperatures and higher effect speeds. Temperatures are generally far beneath the liquefying point of the splashing powders, which takes into consideration sans oxide stores with an immaterial warming impact on the shower materials and substrates. Lingering stresses in these stores are of the compressive sort, which is valuable in manufacturing thick stores. An enormous number of materials have been effectively stored, for example, Cu and its compounds, Al and its combinations, metal composites, metal-earthenware composites, Inconel 718, Ti and Ti6Al4V. Be that as it may, throughout the long term, it has remained truly challenging to create high-strength Ti6Al4V stores, albeit in situ shot peening helping cold splash or post-treatment with heat treatment and thermostatic isostatic strain can work on their densities.

As per the writing, the expansion in speed of titanium composite particles considers the manufacture of a moderately thick store. It has been shown that to accomplish a high molecule speed, particularly planned Laval spouts with a merged segment and a disparate area are important for a CSAM framework. The interior components of the Laval spout influence the molecule speed increase. A ton of pertinent works have been performed, as displayed in Table 1. The majority of the distributed investigations center around the streamlining of the spout extension proportion (the proportion of exit to throat cross-sectional region) and dissimilar length. A few scientists have utilized high-pressure cold splash frameworks to get ready unadulterated titanium coatings to safeguard magnesium combinations. Furthermore, a few researchers have concentrated on the impact of spout cross over speed and deadlock.

Material	Inlet Diameter (mm)	Convergent Length (mm)	Throat Diameter (mm)	Divergent Length (mm)	Exit Diameter (mm)	Experimental Validation
Cu	17	30	2.2	80–440	4.4, 6.22, 7.62	N
Cu	8	10	2	40	2, 3, 4, 5, 6, 7, 8	Y
316L stainless	18.2	54	2.7, 5.4	67.6, 120, 270	10.4-12.4	Y
Polymer	9.8	4.44	2.66	133.68	6.3	Y
N/A	14	20	2.7	59.9, 69.9, 79.9, 89.9	8.36	N
Al	N/A	17, 22, 27, 32, 42, 57	2.7	42, 57, 67, 72, 77, 82	4.32, 5.58, 6.84, 8.5	N
Al	N/A	N/A	0.5	20	1	N
Al	N/A	N/A	0.5	20	1	Y
Ti	10	5	0.8	25	1.5	Y
Ti	N/A	43.6	2.7	129	6.6	Y
Ti	10	15.5, 20, 30	1, 1.34	180, 190	3, 4	Y

Table 1: Different studies on the internal dimensions of the Laval nozzle

Note: Y: yes, N: no, and N/A: not available

Distance on Ti covering structure. The different area mostly influences the speed increase of the particles. Less investigations have zeroed in on the impact of concurrent length on Al powders. Micronozzles for energy-productive showering have been examined with Al and Ti powders. Single Ti molecule influence conduct has been explored in the affidavit of Ti . The impact of merged length has been contemplated, and single-pass Ti coatings have been delivered for various spouts. Among the conceivable interaction boundaries, molecule speed and affidavit proficiency have been considered. Different metal materials, like Cu, Al, Ti, and Ti6Al4V, have broadly unique properties, as displayed in Table 2. Thus, the basic speeds of Cu, Al, Ti, and Ti6Al4V for CSAM are altogether different from 451 m/s to 1013 m/s at room temperature (20 °C). The Laval spouts normally utilized to create stores of Cu, Al, and their composites have a short joined length (scope of 5-57 mm in Table 1). Titanium and its combinations have a lot of lower warm conductivities and better return qualities contrasted with Cu and Al, which isn't helpful for heat move in powder particles.

Material	Density (kg/m^3)	Thermal Conductivity (W/m/K)	Heat Capacity (J/kg/K)	Melting Point (°C)	Yield Strength (MPa)	Ultimate Strength (MPa)	Critical Velocity for CSAM (m/s)
Cu	8880	398	386	660	90	210	451
Al	2688	237	905	933	44	80	482
Ti	4506	21.9	522	1680	140	220	712
Ti6Al4V	4420	7.6	537	1660	880	950	1013

Table 2: Material properties

Subsequently, it is important to explore spout calculations for titanium combination particles. The nature of the store is subject to a few factors of the inflight molecule when it influences on the substrate, molecule speed, and temperature. In [34], a long merged segment along with a proper spout unique segment was viewed as helpful to the temperature of titanium compound particles. Titanium amalgam particles might go through extreme plastic misshapening at high speed and temperature during CSAM. The synergetic impacts of high speed and temperature consider great mechanical interlocking and metallurgical holding at the point of interaction, which works on the thickness and mechanical properties. Most of distributed works have not concentrated on the impact of the powder transporter gas with mathematical demonstrating. It is realized that the presentation of powder transporter gas at room temperature unfavorably influences the speed increase and temperature of particles. Subsequently, the powder transporter gas was likewise researched in this review.

II. MATHEMATICAL MODELING

The mathematical model for the spout consolidates the powder infusion, the spout inward design, and the substrate, as displayed in Figure. The propulsive gas enters the concurrent area (Lc) from the bay (gulf breadth, Di). The gas along with the powder flies through the powder infusion to the concurrent area. Heat is traded between room-temperature particles and the transporter gas as well as the

ISSN No:-2456-2165

high-temperature gas in the concurrent area. Afterward, as they go through the throat.

III. NUMERICAL MODELING AND EXPERIMENTAL METHODOLOGY NUMERICAL MODEL

The mathematical model for the spout consolidates the powder infusion, the spout inward construction, and the substrate, as displayed in Figure 1. The propulsive gas enters the merged area (focalized length, Lc) from the gulf (delta width, Di). The gas along with the powder flies through the powder infusion to the merged area. Heat is traded between room-temperature particles and the transporter gas as well as the high-temperature gas in the merged area. Afterward, as they go through the throat (throat measurement, Dt), follow the dissimilar segment (different length, Ld), and leave (leave breadth, De), the Ti6Al4V particles are warmed and advanced in the spout and effect on the substrate to create the store. The external width (D) of the powder infusion pipe is 4 mm and its inside breadth is 2 mm. The substrate is a circle with a thickness of 5 mm and a breadth of 40 mm, while the stalemate distance (SoD) between the spout and the substrate is 30 mm.

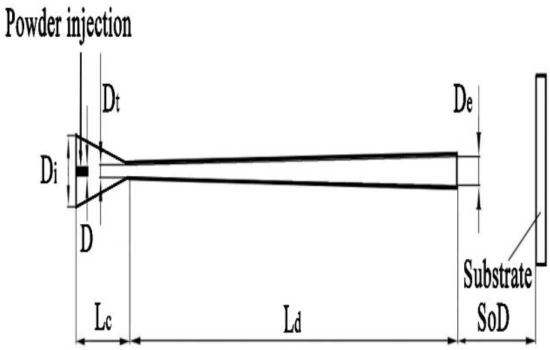

Fig. 1: Nozzle internal dimensions used in the numerical model

The different spout aspects examined in Table 3. As the throat measurement influences gas utilization, taking into account the stock limit of the gas source, two unique spout sizes, one for low gas utilization (Dt = 1.5 mm) and another addressing standard size (Dt = 2.7 mm), were considered. In our past examinations, the spout was ideally planned by coupling inside aspects and gas stream so the particles travel to arrive at a satisfactory speed increase [34,35]. In light of these discoveries, the enhanced spout bay breadth (Di = 20 mm), appropriate extension proportion, and long unique area were chosen for this review. The little throat-breadth spouts were of two kinds, the first, named 1.5-30, had a focalized length of 30 mm, and the subsequent one, named 1.5-65, had a concurrent length of 65 mm. The Ld and De were 170 and 3.6 mm, separately. The enormous throat measurement spouts were of three kinds, named 2.7-30 (Lc = 30 mm), 2.7-40 (Lc = 40 mm), and 2.7-90 (Lc = 90 mm). The Ld and De were 210 mm and 6 mm, separately. Nitrogen (N_2) was utilized as the powder transporter gas as well as the propulsive gas. The propulsive gas strain and temperature were 3 MPa and 550 °C, individually.

The mathematical investigation suite FLUENT 15.6 was utilized for the reproductions to work out the stream field around the spout utilizing a two-layered axisymmetric model, which was decided to decrease computational burden. As indicated by the previously mentioned model construction, the computation region was isolated into three sections: compression segment, extension area, and external region. A cross section of quadrilateral components was utilized.

Type	D_i	L_c	D_t	L_d	D_e	Total Length
1.5–30		30	1.5	170	3.6	200
1.5–65		65				235
2.7–30	20	30				240
2.7–40		40	2.7	210	6	250
2.7–90		90				300

Both the spout wall and the substrate were defined as non-slip limits, and the warm condition was set as adiabatic. The powder particles were taken care of from the focal point of the spout entrance, and the spans of the comparing particles were set by various examination centers. The particles were good to go as round particles, the underlying rate was set to 15 m/s, and the underlying temperature was set to 300 K. In the arrangement cycle, a thickness based coupled solver and a second-request upwind discrete plan were utilized, and the consistent state arrangement was utilized as the outcome. Furthermore, the impact of particles on the stream field was disregarded in the arrangement cycle. The other model boundaries and subtleties have been portrayed in past examinations.

IV. EXPERIMENT MATERIALS AND METHOD

The splash powder utilized was industrially accessible Ti6Al4V powder ready by latent gas atomization. The molecule morphology and size dissemination are displayed in Figure 2. Ti6Al4V particles are circular, with a typical width of 25 µm. Moreover, the test utilizes ten Ti6Al4V plates of a similar size as the substrate, with each plate being 50 mm long, 50 mm wide, and 2 mm thick. 30 minutes before the CSAM try, the substrates were sandblasted utilizing Al_2O_3 powder to eliminate oxides and pollutants on a superficial level.

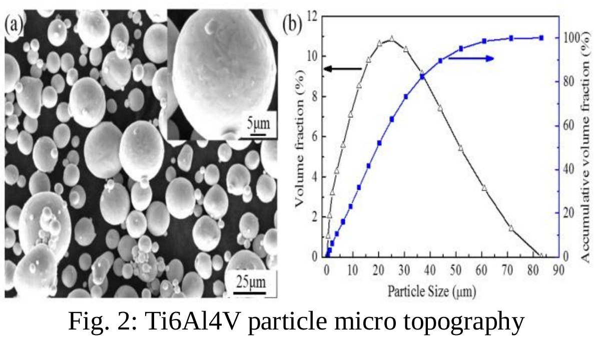

Fig. 2: Ti6Al4V particle micro topography (a) and size distribution (b).

ISSN No:-2456-2165

The five unique spouts and stores made by the 2.7-90 spout are displayed in Figure 3. Treated steel 304 (Northwest Nonferrous Metals Research Institute, Xi'an, China) was chosen as the metal material and the spouts were ready by mechanical handling. The interior sizes of five distinct spouts were machined by the aspects recorded in Table 3, and the presence of the five unique spouts is displayed in Figure 3a. The Ti6Al4V stores were created utilizing an exceptionally grown high-pressure CSAM framework; the spout was as displayed in Figure 3b. The boundaries chose were equivalent to those utilized in the reenactments. The powder taking care of rate was 3 rpm, and the spout travel speed was 40 mm/s. The single-pass stores created by 2.7-90 spout are displayed in Figure 3c. The microstructure of the stores was contemplated with the TESCAN tungsten fiber checking electron magnifying instrument (Brno, Czech Republic), while tests were ready by crushing and cleaning to quantify their width and thickness. The THV-1D Vickers hardness analyzer (TIME, Beijing, China), was utilized to test the microhardness of the coatings. Five focuses were tried for each covering, and the typical worth was taken as the microhardnessof the covering.

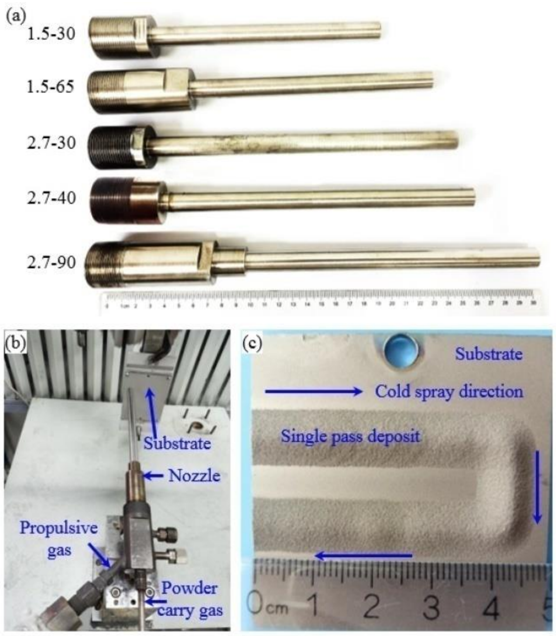

Fig. 3: Five different nozzles (a), 2.7–90 nozzle and substrate (b), and single-pass deposits made using the 2.7–90 nozzle (c).

V. RESULTS AND DISCUSSION

A. Gas Flow, Gas Temperature, and Particle Temperature:

The gas temperature distribution in the nozzle convergent section for various convergent lengths is shown in Figure 4. The powder carrier gas is introduced at room temperature and remains in the center of the nozzle, while the high-temperature propulsive gas fills the rest of the nozzle volume. Those flows begin to mix at about 5 mm inside the inlet. As the convergent section becomes long, the temperature of axial gas rises, and the gas flow becomes evenly distributed.

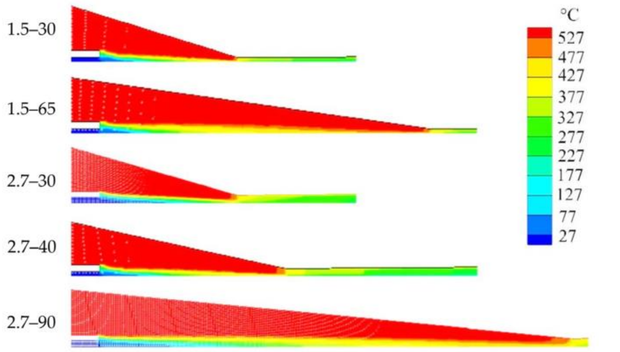

Fig. 4: Gas temperature distribution in the nozzle for various convergent section lengths.

The gas temperature along the nozzle axis was calculated as shown in Figure 5. It increases significantly in the convergent section reaching a maximum close to the throat. This causes the gas to expand and decreases its temperature in the divergent section. When keeping the throat diameter constant, axial gas temperature increases with convergent length, as the mixed gas shows an improved exchange of heat. This would be beneficial for the temperature of the particle. Molecule temperatures under various spout conditions are displayed in Figure 6. As should be visible in Figure 6a, it rises quickly not long after powder infusion, arrives at a greatest at the throat, and afterward diminishes slowly over the dissimilar segment. At the point when the united length is long, the molecule temperature at the spout throat increments, as displayed in Figure 6b. The molecule influence temperature increments from 221.3 to 296.1 °C when the merged length increments from 30 to 65 mm for the 1.5 mm throat. The molecule influence temperature increments from 195.7 to 271.6 °C when the spout focalized segment changes from 30 to 90 mm for the 2.7 mm throat. Particles at high temperatures are bound to turn out to be delicate and plastically misshape during CSAM. In our past examinations, we showed that molecule size influences molecule speed increase. The determined molecule temperatures of various measured particles upon influence on the substrate are displayed in Figure 7.

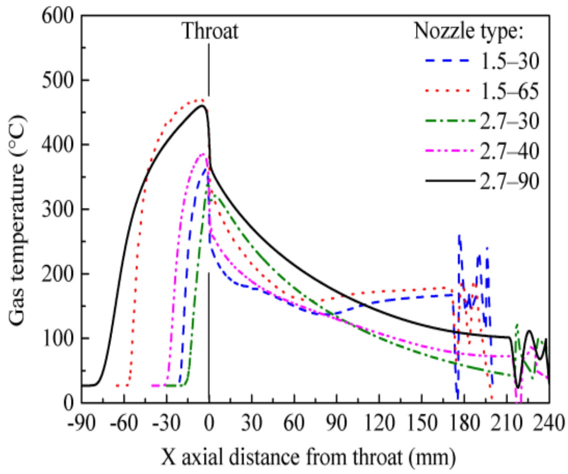

Fig. 5: Gas temperature profile along the nozzle axis.

ISSN No:-2456-2165

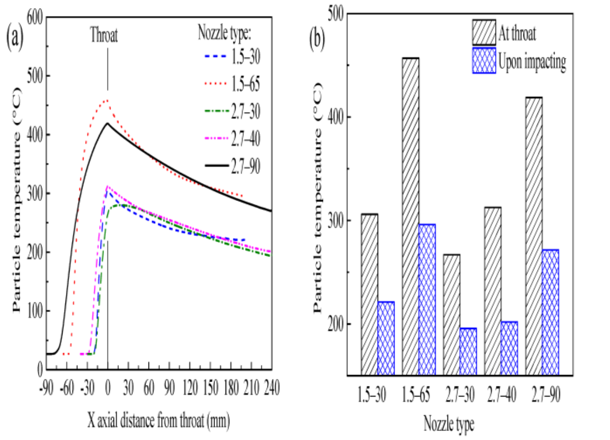

Fig. 6: Particle temperature along with the nozzle axis (a), and the particle temperatures at the nozzle throat and upon influence on the substrate (b). Note: molecule width is 25 µm.

The effect temperature of the 5 µm molecule is the most reduced among the three sizes of particles for a similar spout. Furthermore, when the spout throat is 1.5 mm, the effect temperature of the 45 µm molecule increments from 196.6 °C to 331.5 °C with an expansion in merged length from 30 mm to 65 mm. At the point when the spout throat is 2.7 mm, the effect temperature of the 45 µm molecule ascends from 176.5 °C to 292.5 °C with an expansion in merged length from 30 mm to 90 mm. It ought to be noticed that when the joined length is more limited (either 40 mm or 30 mm, as in the 1.5-30 case, the 2.7-30 case, and the 2.7-40 case), the effect temperature of the 25 µm molecule is the might demonstrate that the connection between molecule temperature and molecule measurement first increments and afterward diminishes. To break down and check this most noteworthy.

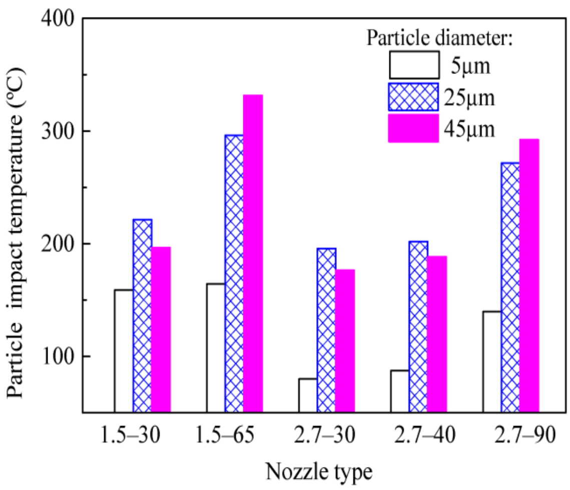

Fig. 7: Particle temperatures upon impact on the substrate

This fascinating relationship, an extensive variety of molecule measurements was utilized, from 5 to 85 µm, with an addition of 20 µm, on account of the 2.7-90 spout. The molecule temperatures alongside the spout hub and the flying time are displayed in Figure 8a,b, separately. Like Figure 6a, the molecule temperature increments and afterward diminishes with the greatest at the spout throat for all molecule distances across, right off the bat. expanded molecule measurement, more extreme temperature climb in the focalized area, and uncommon drop in the unique segments can be noticed (Figure 8a). The 5 µm molecule yields the most significant length of time in the spout, while the 85 µm molecule yields the briefest time, as shown in Figure 8b,c. In the mean time, the 45 µm molecule shows the most noteworthy effect temperature, as displayed in Figure 8c. This outcome could be brought about by the different speed increase ways of behaving of various particles in both the joined and disparate pieces of the spout. Thus, to have the most elevated conceivable effect temperature of a given powder (having a specific molecule size dispersion), a reasonable spout focalized segment is important.

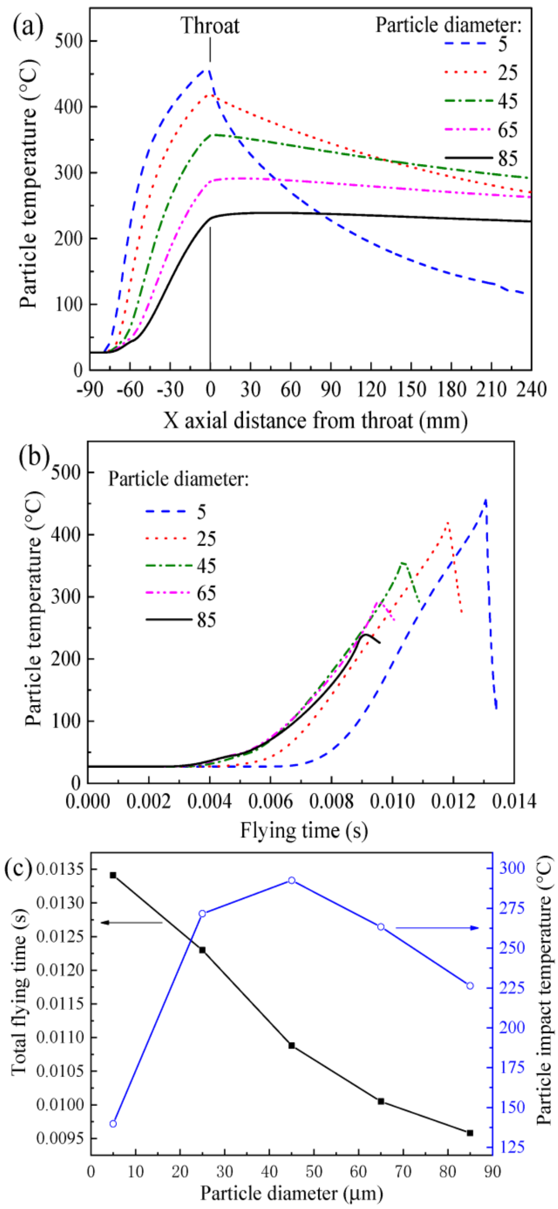

Fig. 8: Molecule temperature profiles along the spout pivot (a) and with flying time (b), and the progressions in molecule all out flying time and temperature with molecule measurement (c) on account of spout 2.7-90.

ISSN No:-2456-2165

B. Gas Velocity and Particle Acceleration

The gas speed along the spout pivot is displayed in Figure 9. As the gas moves through the throat, it speeds up fundamentally in the different segment. At the point when the length of the joined area expands, the gas speed turns out to be marginally higher. The determined molecule motor energy along the spout pivot for different spouts is displayed in Figure 10. The expansion in the molecule motor energy impact is like that of gas. In past examinations, molecule speed increase has been viewed as subject to the unique length, with particles having a higher speed with longer dissimilar segments. The molecule dynamic energy increments when the length of the merged area expansions in this review. This is another finding, recommending that the focalized segment additionally has some gainful effect on molecule speed increase.

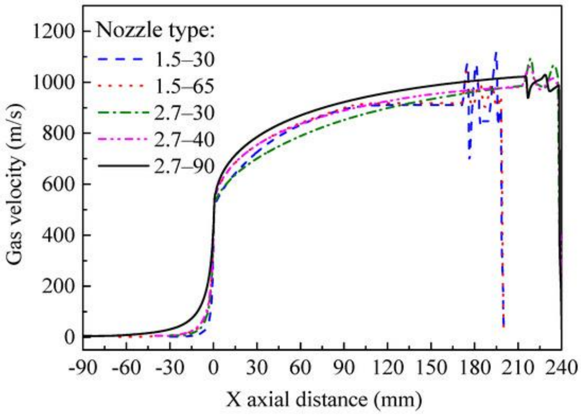

Fig. 9: Gas velocity along the nozzle axis.

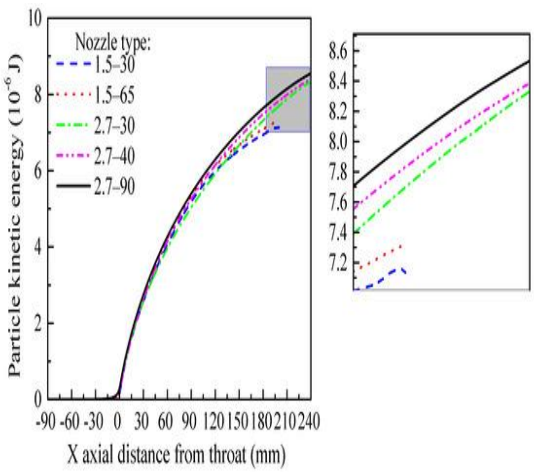

Fig. 10: Particle kinetic energy along with the nozzle axis. Please note that the particle diameter is 25 µm.

The kinetic energies of particles with various diameters upon impact on the substrate are shown in Figure 11. It can be seen that for the three particle sizes studied in this work, the particle kinetic energy before impact increases slightly with increasing convergent length, while the 45 µm particle reaches higher kinetic energy than the 25 µm and 5 µm particles. Particles with higher kinetic energy deform plastically in a more extensive manner. The five different single-pass stores and their widths are displayed in Figure 12. The store in the 1.5-30 case in Figure 12a is around 4 mm in width with unpleasant edges; as the merged length increments from 30 to 65 mm, the width builds a bit, from 4.1 to 4.5 mm, and the harshness of the edges is diminished, as displayed in Figure 12b. At the point when the spout throat breadth is 2.7 mm, the concurrent length increments from 30 to 90 mm, as displayed in Figure 12c-e; the width of the single-pass store likewise increments from 8.2 to 8.9 mm, the edges of the store change from harsh to smooth, and the molecule conveyance on the single covering surface is generally uniform. It tends to be finished up from Figure 12 fthat as the length of the spout united segment builds, the width of the store increments.

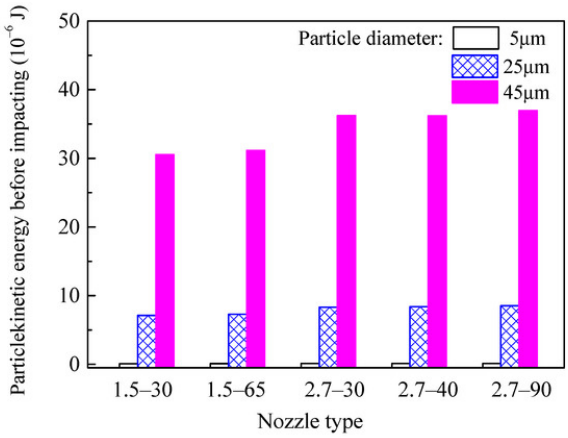

Fig. 11: The kinetic energy of different-sized particles upon impact on the substrate. Note: that the kinetic energy value of the 5 µm particles is between 1.02 × 10−7 J and 1.22 × 10−7 J.

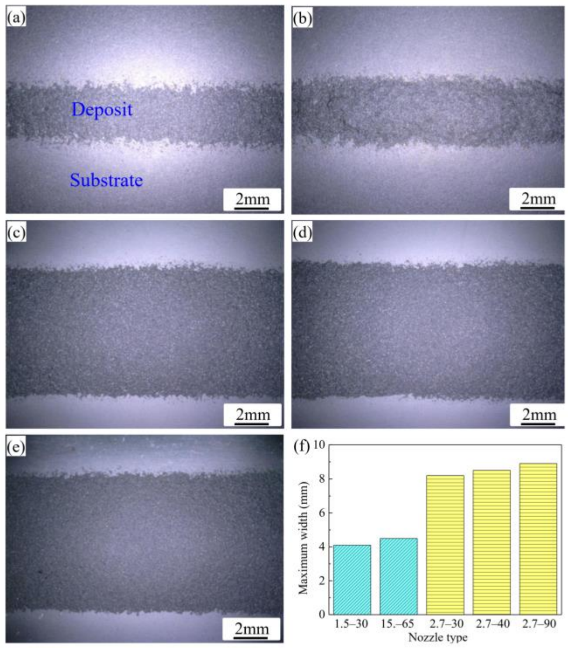

Fig. 12: The surface morphology and maximum width of five different single-pass deposits: (a) 1.5–30; (b) 1.5–65; (c) 2.7–30; (d) 2.7–40; (e) 2.7–90; and (f) maximum width.

The cross-sectional microstructure of the single-pass deposit is shown in Figure 13. The deposits with an arched shape are on the substrate, and the deposit and corresponding substrate are well combined. The deposits in the 1.5–30 cases are loose, with many tiny pores. In

ISSN No:-2456-2165

contrast, the thickness of the deposit in the 1.5–65 case increases, the zone of the deposit close to the substrate is dense, and its upper zone is relatively loose, which is because of the “tamping effect” in the CSAM process [51], as the following particles further tamp the deposited ones, increasing the deposit density. A similar phenomenon can be observed in the 2.7–30, 2.7–40, and 2.7–90 cases: as the nozzle convergent section becomes longer, the microstructure changes from porous to dense, and the density increases.

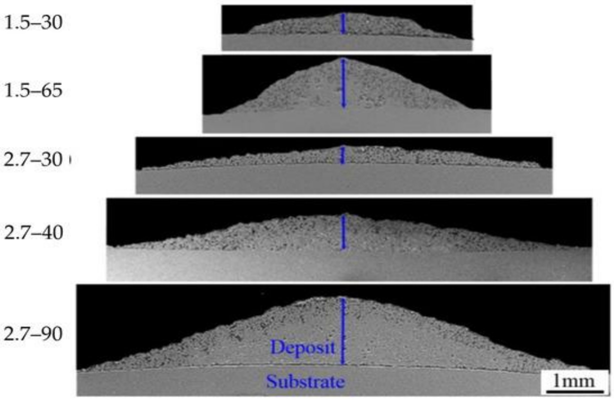

Fig. 13.Cross-sectional microstructure of single-pass deposits

The single-pass store in the 2.7-90 case was sanded and cleaned to notice its microstructure. Figure 14 shows the cross-sectional microstructure of the store. What's more, Figure 15 shows a high-amplification picture of its microstructure, alongside region check consequences of minuscule chose regions. There are voids and pores in the store. The porosity of the covering acquired by the area strategy is 28.88%. Three particles are bound together, as displayed in Figure 14b and Figure 15a,b, where the three particles are named P1, P2, and P3. It tends to be seen that there are no voids on the holding point of interaction, showing that the particles go through incredible plastic distortion during the virus showering process, which advances the tight holding between particles. The region check consequences of little chosen regions An and B are displayed in Figure 15c,d.

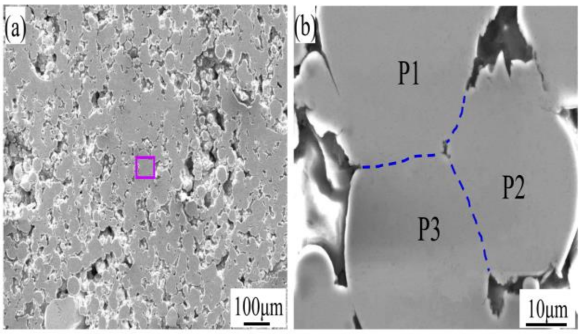

Fig. 14: Cross-sectional microstructure of single-pass deposit in 2.7–90 case: (a) low-magnification scanning electron microscopy; (b) high-magnification scanning electron microscopy in the purple solid frame of (a). Note: the blue dashed line indicates the bonding interface between particles.

Moreover, it was observed that the particles are chiefly made out of titanium (Ti), aluminum (Al), and vanadium (V). Noticing the appropriation of oxygen components, it very well may be seen that the substance of oxygen elements is very low, and there is no enrichment in the scanning area, indicating that the particles were not oxidized during the CSAM process.

The most extreme thickness of the store is utilized as a pointer to mirror the affidavit productivity. The most extreme thickness in the cross-sectional microstructure of the single-pass store is displayed in Figure 16. The microhardness is utilized to portray the mechanical properties of the store.

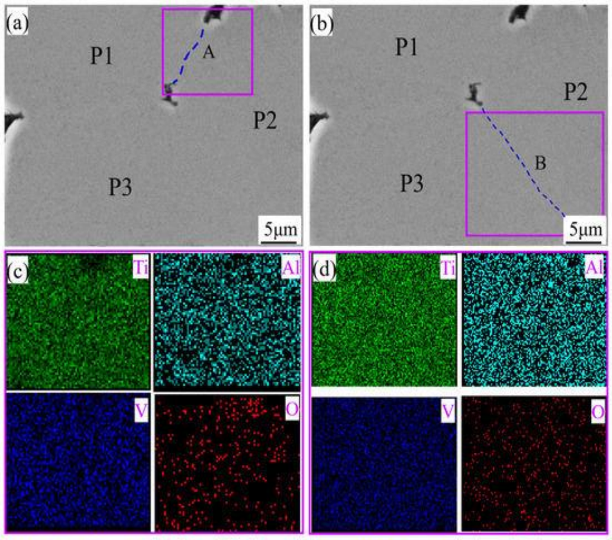

Fig. 15: The high amplification microstructure of the store in the 2.7-90 case: (a) high-amplification filtering electron microscopy and little determination region A; (b) high-amplification examining electron microscopy and minuscule choice region B; (c) region examine consequences of small chosen region A; (d) region filter consequences of little chosen region B. Note: the blue ran line demonstrates the holding point of interaction between particles.

Figure 17 presents a histogram of the microhardness of the single-pass store. At the point when the spout throat width is 1.5 mm, the focalized length increments from 30 mm to 65 mm, and the most extreme thickness of the single-pass store increments from 378 µm to 878 µm. The microhardness increments from 265 HV to 297 HV. At the point when the spout throat is 2.7 mm, the focalized length increments from 30 mm to 90 mm, and the greatest thickness of a solitary pass store increments from 343 µm to 1179 µm. The microhardness increments from 247 HV to 324 HV. As the concurrent segment turns out to be longer, particles accomplish higher speed and temperatures, the affidavit proficiency expands altogether, and stores become thick and have high microhardness.

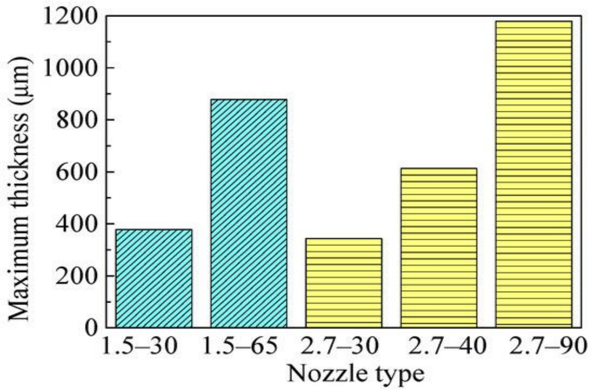

Fig. 16: The maximum thickness achieved with single-pass deposits

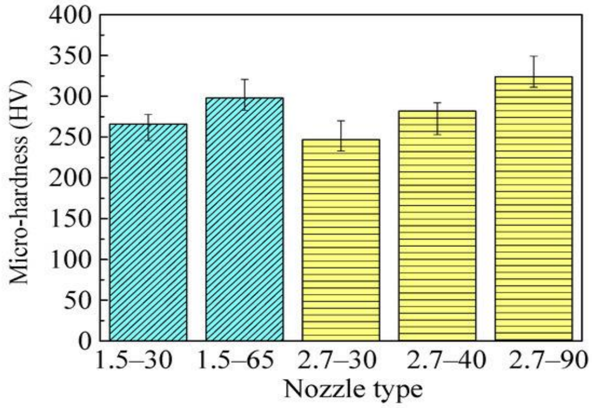

Fig. 17: The microhardness of single-pass deposits

VI. CONCLUSIONS

The temperature and speed of the gas, as well as Ti6Al4V particles, were concentrated on in five unique spouts during the CSAM cycle through mathematical displaying. The aftereffects of these recreations were approved with single-pass stores. The accompanying ends can be drawn:

The temperature of gas and particles increments with expanding length of the spout united segment, while the molecule temperatures at the spout throat and upon influence on the substrate both ascent, which is of advantage for the conditioning of particles, as well as their resulting plastic disfigurement. The connection between the molecule influence temperature and molecule width first increments, and afterward diminishes.

Particles going inside longer merged segments have higher speeds at the throat, and are then accordingly advanced by the growing gas in the disparate segment. Thus, they arrive at higher active energy at influence, which brings about more serious plastic distortion during CSAM. Molecule influence motor energy is decidedly connected with molecule size.

With a more extended focalized segment of the spout, the edges of the single-pass stores change from harsh to smooth, and store width increments. What's more, the store microstructure changes from permeable to thick, and the particles in the 2.7-90 store are firmly reinforced. The expansion in the most extreme thickness and microhardness of the store demonstrate the superior testimony proficiency and mechanical properties.

REFERENCES

[1.] Raoelison, R.N.; Verdy, C.; Liao, H. Cold gas dynamic spray additive manufacturing today: Deposit possibilities, technological solutions and viable applications. Mater. Des. 2017, 133, 266–287. [Google Scholar] [CrossRef]

[2.] Yin, S.; Cavaliere, P.; Aldwell, B.; Jenkins, R.; Liao, H.; Li, W.Y.; Lupoi, R. Cold spray additive manufacturing and repair: Fundamentals and applications. Addit. Manuf. 2018, 21, 628–650. [Google Scholar] [CrossRef]

[3.] Yin, S.; Cizek, J.; Cupera, J.; Hassani, M.; Luo, X.T.; Jenkins, R.; Xie, Y.C.; Li, W.Y.; Lupoi, R. Formation conditions of vortex-like intermixing interfaces in cold spray. Mater. Des. 2021, 200, 109444. [Google Scholar] [CrossRef]

[4.] Xie, X.; Ma, Y.; Chen, C.; Ji, G.; Verdy, C.; Wu, H.; Chen, Z.; Yuan, S.; Normand, B.; Yin, S.; et al. Cold spray additive manufacturing of metal matrix composites (MMCs) using a novel nano-TiB2-reinforced 7075Al powder. J. Alloys Compd. 2020, 819, 152962. [Google Scholar] [CrossRef]

[5.] Li, W.Y.; Assadi, H.; Gaertner, F.; Yin, S. A Review of advanced composite and nanostructured coatings by solid-state cold spraying process. Crit. Rev. Solid State Mater. Sci. 2018, 44, 109–156. [Google Scholar] [CrossRef]

[6.] Li, W.Y.; Cao, C.C.; Yin, S. Solid-state cold spraying of Ti and its alloys: A literature review. Prog. Mater. Sci. 2019, 110, 100633. [Google Scholar] [CrossRef]

[7.] Bagherifard, S.; Monti, S.; Zuccoli, M.V.; Riccio, M.; Kondás, J.; Guagliano, M. Cold spray deposition for additive manufacturing of freeform structural components compared to selective laser melting. Mater. Sci. Eng. A. 2018, 721, 339–350. [Google Scholar] [CrossRef]

[8.] Feng, Y.; Li, W.Y.; Guo, C.; Gong, M.; Yang, K. Mechanical property improvement induced by nanoscaled deformation twins in cold-sprayed Cu coatings. Mater. Sci. Eng. A. 2018, 727, 119–122. [Google Scholar] [CrossRef]

[9.] Li, W.Y.; Wu, D.; Hu, K.W.; Xu, Y.X.; Yang, X.W.; Zhang, Y. A comparative study on the employment of heat treatment, electric pulse processing and friction stir processing to enhance mechanical properties of cold-spray-additive-manufactured copper. Surf. Coat. Technol. 2021, 409, 126887. [Google Scholar] [CrossRef]

[10.] Huang, C.; Li, W.Y.; Feng, Y.; Xie, Y.; Planche, M.-P.; Liao, H.; Montavon, G. Microstructural evolution and mechanical properties enhancement of a cold-sprayed Cu Zn alloy coating with friction stir processing. Mater. Charact. 2017, 125, 76–82. [Google Scholar] [CrossRef]

[11.] Liu, T.; Leazer, J.D.; Menon, S.K.; Brewer, L.N. Microstructural analysis of gas atomized Al-Cu alloy feedstock powders for cold spray deposition. Surf.

Coat. Technol. 2018, 350, 621–632. [Google Scholar] [CrossRef]
[12.] Zhao, H.; Tan, C.; Yu, X.; Ning, X.; Nie, Z.; Cai, H.; Wang, F.; Cui, Y. Enhan-ced reactivity of Ni-Al reactive material formed by cold spraying combined with cold-pack rolling. J. Alloys Compd. 2018, 741, 883–894. [Google Scholar] [CrossRef]
[13.] Liu, T.; Leazer, J.D.; Brewer, L.N. Particle deformation and microstructure evolution during cold spray of individual Al-Cu alloy powder particles. Acta Mater. 2019, 168, 13–23. [Google Scholar] [CrossRef]
[14.] Zeng, G.; Zahiri, S.H.; Gulizia, S.; Chen, Y.; Xu, C.; Chen, X.-B.; Cole, I. A comparative study of cell growth on a cold sprayed Ti-Ta composite. J. Alloys Compd. 2020, 826, 154014. [Google Scholar] [CrossRef]
[15.] Li, W.Y.; Guo, X.P.; Verdy, C.; Dembinski, L.; Liao, H.L.; Coddet, C. Improvement of microstructure and property of cold-sprayed Cu-4 at.%Cr-2 at.%Nb alloy by heat treatment. Scripta Mater. 2006, 55, 327–330. [Google Scholar] [CrossRef]
[16.] Wu, H.; Zhang, L.; Liu, C.; Mai, Y.; Zhang, Y.; Jie, X. Deposition of Zn-G/Al composite coating with excellent cathodic protection on low-carbon steel by l-ow-pressure cold spraying. J. Alloys Compd. 2020, 821, 153483. [Google Scholar] [CrossRef]
[17.] Yang, K.; Li, W.Y.; Niu, P.; Yang, X.; Xu, Y. Cold sprayed AA2024/Al2O3 metal matrix composites improved by friction stir processing: Microstructure characterization, mechanical performance and strengthening mechanisms. J. Alloys Compd. 2018, 736, 115–123. [Google Scholar] [CrossRef]
[18.] Huang, C.J.; Li, W.Y.; Zhang, Z.; Fu, M.; Planche, M.-P.; Liao, H.; Montavon, G. Modification of a cold sprayed SiCp/Al5056 composite coating by friction stir processing. Surf. Coat. Technol. 2016, 296, 69–75. [Google Scholar] [CrossRef]
[19.] Wang, X.; Zhang, L.; Zhou, X.; Wu, W.; Jie, X. Corrosion behavior of Al2O3-reinforced graphene encapsulated Al composite coating fabricated by low pressure cold spraying. Surf. Coat. Technol. 2020, 386, 125486. [Google Scholar] [CrossRef]
[20.] Yang, K.; Li, W.Y.; Xu, Y.X.; Yang, X.W. Using friction stir processing to augment corrosion resistance of cold sprayed AA2024/Al2O3 composite coatings. J. Alloys Compd. 2019, 774, 1223–1232. [Google Scholar] [CrossRef]
[21.] Ma, W.; Xie, Y.; Chen, C.; Fukanuma, H.; Wang, J.; Ren, Z.; Huang, R. Microstructural and mechanical properties of high-performance Inconel 718 alloy by cold spraying. J. Alloys Compd. 2019, 792, 456–467. [Google Scholar] [CrossRef]
[22.] Luo, X.T.; Yao, M.L.; Ma, N.; Takahashi, M.; Li, C.J. Deposition behavior, microstructure and mechanical properties of an in-situ micro-forging assisted cold spray enabled additively manufactured Inconel 718 alloy. Mater. Design. 2018, 155, 384–395. [Google Scholar] [CrossRef]
[23.] Sun, W.; Bhowmik, A.; Tan, A.W.Y.; Li, R.; Xue, F.; Marinescu, I.; Liu, E. Improving microstructural and mechanical characteristics of cold-sprayed Inconel 718 deposits via local induction heat treatment. J. Alloys Compd. 2019, 797, 1268–1279. [Google Scholar] [CrossRef]
[24.] Aydin, H.; Alomair, M.; Wong, W.; Vo, P.; Yue, S. Cold spray ability of mixed commercial purity Ti plus Ti6Al4V metal powders. J. Therm. Spray Technol. 2017, 26, 360–370. [Google Scholar] [CrossRef]
[25.] Tan, A.W.Y.; Sun, W.; Phang, Y.P.; Dai, M.; Marinescu, I.; Dong, Z.; Liu, E. Effects of traverse scanning speed of spray nozzle on the microstructure and mechanical properties of cold-sprayed Ti6Al4V coatings. J. Therm. Spray Technol. 2017, 26, 1484–1497. [Google Scholar] [CrossRef]
[26.] Sun, W.; Tan, A.W.Y.; Marinescu, I.; Toh, W.Q.; Liu, E. Adhesion, tribological and corrosion properties of cold-sprayed CoCrMo and Ti6Al4V coatings on 6061-T651 Al alloy. Surf. Coat. Technol. 2017, 326, 291–298. [Google Scholar] [CrossRef]
[27.] Munagala, V.N.V.; Imbriglio, S.I.; Chromik, R.R. The influence of powder properties on the adhesion strength and microstructural evolution of cold sprayed Ti6Al4V single splats. Mater. Lett. 2019, 244, 58–61. [Google Scholar] [CrossRef]
[28.] Li, W.Y.; Yang, K.; Yin, S.; Yang, X.W.; Xu, Y.X.; Lupoi, R. Solid-state additive manufacturing and repairing by cold spraying: A review. J. Mater. Sci. Technol. 2018, 34, 440–457. [Google Scholar] [CrossRef]
[29.] Li, W.Y.; Cao, C.C.; Wang, G.Q.; Wang, F.F.; Xu, Y.X.; Yang, X.W. 'Cold spray +' as a new hybrid additive manufacturing technology: A literature review. Sci. Technol. Weld. Join. 2019, 24, 420–445. [Google Scholar] [CrossRef]
[30.] Luo, X.T.; Wei, Y.K.; Wang, Y.; Li, C.J. Microstructure and mechanical property of Ti and Ti6Al4V prepared by an in-situ shot peening assisted cold spraying. Mater. Des. 2015, 85, 527–533. [Google Scholar] [CrossRef]
[31.] Zhou, H.X.; Li, C.J.; Yang, H.; Luo, X.T.; Yang, G.; Li, W.Y.; Hussain, T.; Li, C.J. Pores structure change induced by heat treatment in cold-sprayed Ti6Al4V coating. J. Therm. Spray Technol. 2019, 28, 1199–1211. [Google Scholar] [CrossRef]
[32.] Chen, C.; Xie, Y.; Yan, X.; Yin, S.; Fukanuma, H.; Huang, R.; Zhao, R.; Wang, J.; Ren, Z.; Liu, M.; et al. Effect of hot isostatic pressing (HIP) on microstructure and mechanical properties of Ti6Al4V alloy fabricated by cold spray additive manufacturing. Addit. Manuf. 2019, 27, 595–605. [Google Scholar] [CrossRef]
[33.] Yin, S.; Meyer, M.; Li, W.Y.; Liao, H.; Lupoi, R. Gas flow, particle acceleration, and heat transfer in cold spray: A review. J. Therm. Spray Technol. 2016, 25, 874–896. [Google Scholar] [CrossRef]
[34.] Yin, S.; Zhang, M.; Guo, Z.; Liao, H.; Wang, X. Numerical investigations on the effect of total pressure and nozzle divergent length on the flow character and particle impact velocity in cold spraying. Surf. Coat. Technol. 2013, 232, 290–297. [Google Scholar] [CrossRef]

[35.] Li, W.Y.; Li, C.J. Optimal design of a novel cold spray gun nozzle at a limited space. J. Therm. Spray Technol. 2005, 14, 391–396. [Google Scholar] [CrossRef]
[36.] Li, W.Y.; Liao, H.; Douchy, G.; Coddet, C. Optimal design of a cold spray nozzle by numerical analysis of particle velocity and experimental validation with 316L stainless steel powder. Mater. Des. 2007, 28, 2129–2137. [Google Scholar] [CrossRef]
[37.] Alhulaifi, A.S.; Buck, G.A.; Arbegast, W.J. Numerical and experimental investigation of cold spray gas dynamic effects for polymer coating. J. Therm. Spray Technol. 2012, 21, 852–862. [Google Scholar] [CrossRef]
[38.] Belbaki, A.; Mebdoua-Lahmar, Y. Influence of diverging section length on the supersonic jet delivered from micro-nozzle: Application to cold spray coating process. In Applied Mechanics, Behavior of Materials, and Engineering Systems; Boukharouba, T., Pluvinage, G., Azouaoui, K., Eds.; Springer: New York, NY, USA, 2017; pp. 465–473. [Google Scholar]
[39.] Jung, H.B.; Park, J.I.; Park, S.H.; Kim, H.J.; Lee, C.H.; Han, J.W. Effect of the expansion ratio and length ratio on a gas-particle flow in a converging-dive-rging cold spray nozzle. Met. Mater. Int. 2009, 15, 967–970. [Google Scholar] [CrossRef]
[40.] Sova, A.; Okunkova, A.; Grigoriev, S.; Smurov, I. Velocity of the particles accelerated by a cold spray micronozzle: Experimental measurements and numerical simulation. J. Therm. Spray Technol. 2012, 22, 75–80. [Google Scholar] [CrossRef]
[41.] Sova, A.; Smurov, I.; Doubenskaia, M.; Petrovskiy, P. Deposition of aluminum powder by cold spray micronozzle. Int. J. Adv. Manuf. Technol. 2017, 95, 3745–3752. [Google Scholar] [CrossRef]
[42.] Buhl, S.; Breuninger, P.; Antonyuk, S. Optimization of a Laval nozzle for energy-efficient cold spraying of microparticles. Mater. Manuf. Processes. 2017, 33, 115–122. [Google Scholar] [CrossRef]
[43.] Faizan-Ur-Rab, M.; Zahiri, S.H.; King, P.C.; Busch, C.; Masood, S.H.; Jahedi, M.; Nagarajah, R.; Gulizia, S. Utilization of titanium particle impact location to validate a 3D multicomponent model for cold spray additive manufacturing. J. Therm. Spray Technol. 2017, 26, 1874–1887. [Google Scholar] [CrossRef]
[44.] Lupoi, R. Current design and performance of cold spray nozzles: Experimental and numerical observations on deposition efficiency and particle velocity. Surf. Eng. 2013, 30, 316–322. [Google Scholar] [CrossRef]
[45.] Daroonparvar, M.; Kasar, A.-K.; Khan, M.-U.-F.; Menezes, P.-L.; Kay, C.-M.; Misra, M.; Gupta, R.-K. Improvement of wear, pitting corrosion resistance and repassivation ability of mg-based alloys using high pressure cold sprayed (HPCS) commercially pure-titanium coatings. Coatings 2021, 11, 57. [Google Scholar] [CrossRef]